

SHOULDER AND ELBOW JOINT ANGLE ESTIMATION FOR UPPER LIMB REHABILITATION TASKS USING LOW-COST INERTIAL AND OPTICAL SENSORS

ALIREZA ALIZADEGAN

*Mechanical Engineering Department
University of British Columbia, Vancouver, BC V6T1Z4, Canada
a.r.alizadegan@gmail.com*

SAEED BEHZADIPOUR*

*Mechanical Engineering Department
Sharif University of Technology, Azadi St. Tehran, Iran
behzadipour@sharif.edu*

Received 22 December 2014

Revised 19 October 2015

Accepted 4 April 2016

Published 10 June 2016

This paper proposes a new method to improve accuracy and real-time performance of inertial joint angle estimation for upper limb rehabilitation applications by modeling body acceleration and adding low-cost markerless optical position sensors. A method based on a combination of the 3D rigid body kinematic equations and Denavit-Hartenberg (DH) convention is used to model body acceleration. Using this model, body acceleration measurements of the accelerometer are utilized to increase linearization order and compensate for body acceleration perturbations. To correct for the sensor-to-segment misalignment of the inertial sensors, position measurements of a low-cost markerless position sensor are used. Joint angles are estimated by Extended Kalman Filter (EKF) and compared with Unscented Kalman Filter (UKF) in terms of performance. Simulations are performed to quantify the existing error and potential improvements achievable by the proposed method. Experiments on a human test subject performing an upper limb rehabilitation task is used to validate the simulation results in realistic conditions.

Keywords: Body acceleration; inertial sensors; joint angle estimation; Kalman filter; rehabilitation; linearization; sensor-to-segment misalignment; markerless optical sensors.

1. Introduction

Physical rehabilitation is one of the leading applications of human motion tracking. In a rehabilitation course, quantitative assessment of the performed tasks is necessary for detection and correction of the pathological movements.¹ Shoulder and

*Corresponding author.

elbow joint angles are one of the most important parameters in quantitative assessment of upper limb tasks.

Currently, marker-based optical sensors can be used to quantify joint angles quite accurately.² Nevertheless, these systems are expensive, are prone to the line-of-sight and skin movement problems.³ Moreover, they require installation of numerous markers on the body and a dedicated studio which hinder their ambulatory usage. Recently, an optical sensor, named KinectTM (<http://www.xbox.com/en-US/kinect>), has been released by Microsoft Inc. This sensor is cheap, markerless, and much simpler to use. However, it is designed for gaming purposes and hence has insufficient accuracy.

The limitations of the optical sensors have encouraged a distinct approach based on wearable inertial sensors.⁴ This technology is based on gyroscopes and accelerometers as sensors. Gyroscopes measure the angular velocity and accelerometers measure the vector sum of gravity and body acceleration. Body acceleration is referred to the component of the acceleration caused exclusively by kinematics of the point to which the accelerometer is attached. In absence of body acceleration, relating the gravity vector in the body reference frame to the gravity vector in the global reference frame leads to the body inclination estimation. This measurement model of the accelerometer is referred to as “Inclinometer model” in this work. This model has been used for static and quasi-static measurements using only an accelerometer^{5–7}; however, if body acceleration is considerable, it imposes perturbations to this model.⁸ Complete orientation information can also be obtained by integrating angular velocity measurement of gyroscopes; however, it is not usable independently because integration quickly accumulates the measurement noise resulting in a drift of 10–25° in 1 min.⁹ Therefore, typically gyroscopes and accelerometers are used together to compensate for each other’s limitations.^{10–12} This measurement model is referred to as “Gyroscope/Inclinometer model” in this work.

So far, inertial motion tracking of human is approached based on two kinematic models: (1) articulated model (2) stick-figure model. Figure 1 shows the schematic of these models.

In the stick-figure model, each segment is considered independently, so there is no means to describe the body acceleration. As a result, methods based on this approach typically use “Gyroscope/Inclinometer model” and body acceleration perturbations are dealt with signal processing approaches. For instance, increasing the accelerometer measurement noise variance can mitigate this error; however, this technique is not typically recommended because it weakens accelerometer’s function in correcting gyroscope’s drift error. In Refs. 15 and 16, the magnitude of the measured acceleration vector is monitored for significant deviations from the gravity. If deviation is not detected, accelerometer measurements are used to correct for the integration drift of the gyroscope; otherwise, they receive a lower weight and the integration drift appears. In a different approach, the accelerometer bias is captured by augmenting the state vector.¹⁷ Another limitation of the “Gyroscope/Inclinometer model” is that it can’t capture information about second derivatives

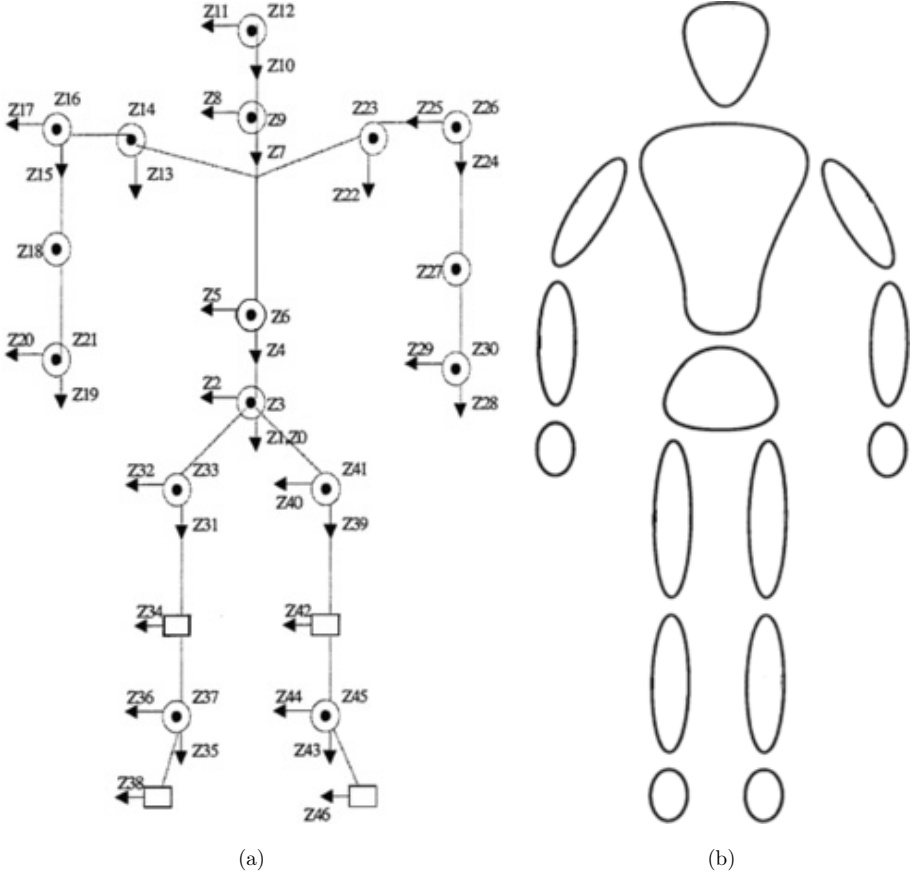


Fig. 1. (a) Articulated kinematic model.¹³ (b) Stick-figure kinematic model.¹⁴

angles existing in the body acceleration which is already measured by the accelerometer. So, methods based on “Gyroscope/Inclinometer model” typically use first-order linearization.

The second category is based on articulated model where human body is considered as an articulated mechanism. Based on this approach, Zhang *et al.*¹⁸ introduced a new approach based on articulated kinematic model of the human body¹³ to consider the elbow abduction/adduction constraint. In this approach the Denavit–Hartenberg (DH) convention is used to model the kinematics of the body.¹⁹ This convention provides a unified context to include prismatic joints as well as revolute joints. This context can be used to formulate rectilinear motion quantities such as body acceleration.

Due to poor control of the upper limb in stroke patients, rehabilitation tasks are characterized by high motion dynamics demanding higher order observability for orientation. Furthermore, this characteristic makes the body acceleration compensation problem even more critical. In the upper limb rehabilitation, slippage of

the soft tissue on the skeleton disrupts correct measurement of the internal/external rotation, unless the upper arm and forearm sensors are located close to the elbow and wrist, respectively. Since in this configuration sensors are located in the most distant location from the origin of the global reference frame, the body acceleration is the highest on the sensors.

In general, inertial technologies suffer from sensor-to-segment misalignment which does not appear in optical technologies. Sensor-to-segment misalignment is caused by calibration and installation errors. Sensor-to-segment misalignment brings about measurement perturbations proportional to the magnitude of the signal. The highly dynamic characteristic of the rehabilitation tasks, coupled with the agility of the upper limb, makes this problem even more critical in this field.

This paper deals with linearization, body acceleration perturbation, and sensor-to-segment misalignment issues by considering upper limb rehabilitation application. Linearization and perturbation problems are dealt by describing body acceleration measurements of accelerometers in the kinematic model. Low-cost markerless optical sensor is used to correct for the sensor-to-segment misalignments. In the following, Sec. 2 describes the method used in this work. In this method, kinematic model of the human upper limb is developed based on the DH convention. Extended Kalman Filter (EKF) is employed for non-linear estimation. Measurement model is developed based on the application of the 3D rigid body kinematic equations to the DH model of the upper limb. Simulation studies are included in Sec. 3 in three subsections. The first subsection studies the effect of linearization order in estimation error. The second subsection examines the impact of position measurement accuracy upon correcting for the sensor-to-segment misalignments perturbation. In the last subsection, the body acceleration compensation is compared with common competing techniques. Section 4 presents the experiments conducted on a human test subject performing an upper limb rehabilitation task. Conclusions in Sec. 5 encompass a brief summary of the method and important results.

2. Method

2.1. Kinematic model

As shown in Fig. 1, the articulated kinematic model typically describes human upper limb by a 3 DOF revolute joint for shoulder and a 2 DOF revolute joint elbow. In this section, mathematical description of this model is presented based on DH convention.¹⁹ Figure 2 depicts the DH description in a configuration for which all joint angles are zero. θ_1 , θ_2 , and θ_3 represent the 3 DOF of the shoulder.

θ_1 reflects the flexion/extension DOF, θ_2 reflects the abduction/adduction DOF, and θ_3 reflects the internal/external rotation in the shoulder. Similarly, θ_4 and θ_5 reflect the flexion/extension and internal/external rotation of the elbow, respectively. Abduction/adduction DOF is not considered for the elbow. l_3 and l_6 designate the upper arm and forearm link dimensions, respectively. Two IMUs are used.

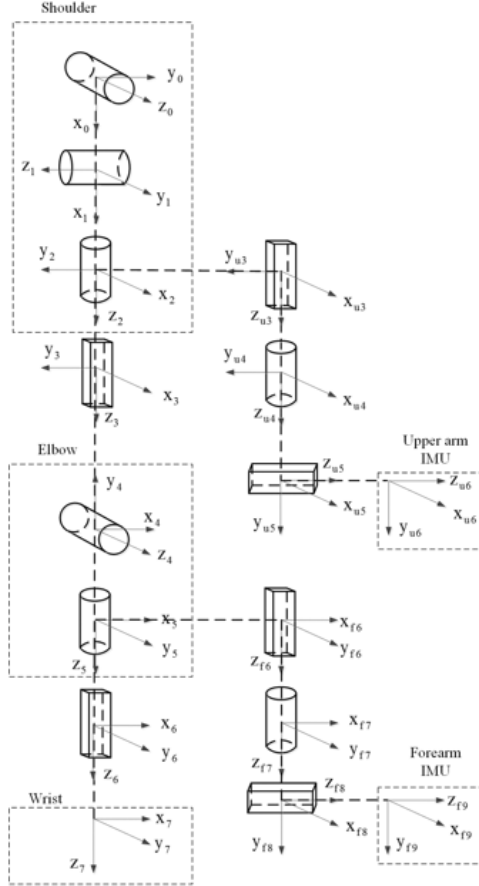


Fig. 2. Upper limb DH kinematic model.

One is placed on the upper arm and the other is placed on the forearm. Kinect is used to measure the position of the elbow and wrist relative to the shoulder in the global reference frame. The degrees of freedom which describe the installation position and orientation of the upper arm and forearm IMU are designated with u and f subscripts, respectively. For instance, the distance of the upper arm and forearm straps from the shoulder and elbow along the internal/external rotation axis are designated by l_{u3} and l_{f6} , respectively. The effective radii of the upper arm and forearm straps are designated by l_{u5} and l_{f8} , respectively. Straps allow a rotational DOF about the internal/external rotation axis. This DOF is designated for the upper arm and forearm straps by θ_{u4} and θ_{f7} , respectively. Based on this model, Tables 1–4 shows the DH table derived for each sensor.

In a DH table γ_i is rotation about z -axis, λ_i is translation along z -axis, β_i is rotation about x -axis, and δ_i is translation along x -axis. The x -axis and z -axis refer to the current axis after each motion.

Table 1. Upper arm IMU DH table.

i	γ_i	λ_i	β_i	δ_i
1	θ_0	0	$\pi/2$	0
2	$\theta_1 + \pi/2$	0	$\pi/2$	0
3	θ_2	0	0	0
4	0	l_{u3}	0	0
5	θ_{u4}	0	$\pi/2$	0
6	0	l_{u5}	0	0

Table 2. Elbow position sensor DH table.

i	γ_i	λ_i	β_i	δ_i
1	θ_0	0	$\pi/2$	0
2	$\theta_1 + \pi/2$	0	$\pi/2$	0
3	θ_2	0	0	0
4	$\pi/2$	l_3	$-\pi/2$	0
5	θ_4	0	$\pi/2$	0

Table 3. Forearm IMU DH table.

i	γ_i	λ_i	β_i	δ_i
1	θ_0	0	$\pi/2$	0
2	$\theta_1 + \pi/2$	0	$\pi/2$	0
3	θ_2	0	0	0
4	$\pi/2$	l_3	$-\pi/2$	0
5	θ_4	0	$\pi/2$	0
6	θ_5	0	0	0
7	0	l_{f6}	0	0
8	$\theta_{f7} + \pi/2$	0	$\pi/2$	0
9	0	l_{f8}	0	0

Table 4. Wrist position sensor DH table.

i	γ_i	λ_i	β_i	δ_i
1	θ_0	0	$\pi/2$	0
2	$\theta_1 + \pi/2$	0	$\pi/2$	0
3	θ_2	0	0	0
4	$\pi/2$	l_3	$-\pi/2$	0
5	θ_4	0	$\pi/2$	0
6	θ_5	0	0	0
7	0	l_6	0	0

2.2. Kalman filter

The state vector is defined as:

$$\mathbf{x} = [\ddot{\boldsymbol{\theta}} \quad \dot{\boldsymbol{\theta}} \quad \boldsymbol{\theta}]. \quad (1)$$

In (1), $\boldsymbol{\theta}$ is the joint vector defined as:

$$\boldsymbol{\theta} = [\theta_0 \quad \theta_1 \quad \theta_2 \quad \theta_4 \quad \theta_5]^T. \quad (2)$$

Joint angle dynamics is modeled with second-order linearization. A first-order Gauss–Markov process (GM-1) is used to describe the second derivative of the joint vector ($\ddot{\boldsymbol{\theta}}$). The first derivative of the joint vector ($\dot{\boldsymbol{\theta}}$) and the joint vector, itself, ($\boldsymbol{\theta}$) are, respectively, obtained by single and double integration of the joint acceleration. The discrete-time process matrix for this model can be written as:

$$\mathbf{F} = \begin{bmatrix} \mathbf{I}_5 & \mathbf{0}_5 & \mathbf{0}_5 \\ t_s \mathbf{I}_5 & \mathbf{I}_5 & \mathbf{0}_5 \\ 0.5t_s^2 \mathbf{I}_5 & t_s \mathbf{I}_5 & \mathbf{I}_5 \end{bmatrix}. \quad (3)$$

In the equation above, t_s is the sampling time-step and \mathbf{I}_n and $\mathbf{0}_n$ are, respectively, identity and zero matrices of dimension n . The process noise covariance matrix is defined as:

$$\mathbf{Q} = \begin{bmatrix} \sigma_{\ddot{\boldsymbol{\theta}}}^2 \mathbf{I}_5 & \mathbf{0}_{5 \times 10} \\ \mathbf{0}_{10 \times 5} & \mathbf{0}_{10} \end{bmatrix}. \quad (4)$$

In (4), $\sigma_{\ddot{\boldsymbol{\theta}}}^2$ is the variance of the process noise describing dynamics of the joint angles.

The measurement is modeled based on application of the DH convention to the 3D rigid body kinematics equations. In this work, it is assumed that the shoulder center of rotation is stationary. This assumption relies on the fact that many upper limb rehabilitation tasks are performed with the trunk being stationary. This frame is set as the global reference frame in the DH convention. The following set of equations describe the global reference frame.

$${}^0\mathbf{p}_0 = \mathbf{0}_{3 \times 1}, \quad (5)$$

$${}^0\boldsymbol{\omega}_0 = \mathbf{0}_{3 \times 1}, \quad (6)$$

$${}^0\dot{\boldsymbol{\omega}}_0 = \mathbf{0}_{3 \times 1}, \quad (7)$$

$${}^0\ddot{\mathbf{p}}_0 = \mathbf{0}_{3 \times 1}, \quad (8)$$

$${}^0\mathbf{g} = g\hat{\mathbf{k}}. \quad (9)$$

Consider the $(i-1)$ th and the i th reference frames in the DH convention. The relative rotation matrix (${}_{i-1}^i\mathbf{R}$) and displacement vector (${}^{i-1}\mathbf{p}_i$) of the i th reference frame with respect to the $(i-1)$ th one, form the homogeneous transformation

which is obtained in terms of the DH parameters γ_i , λ_i , β_i , and δ_i (10):

$${}^{i-1}_i \mathbf{H} = \begin{bmatrix} {}^{i-1}_i \mathbf{R} & {}^{i-1} \mathbf{p}_i \\ \mathbf{0}_{1 \times 3} & 1 \end{bmatrix} = \mathbf{R}_z(\gamma_i) \mathbf{T}_Z(\lambda_i) \mathbf{R}_x(\beta_i) \mathbf{T}_x(\delta_i). \quad (10)$$

Based on the relative rotation matrix and displacement vector, the recursive forward kinematics equations can be formulated as:

$${}^0 \mathbf{p}_i = {}^0 \mathbf{p}_{i-1} = \Pi_1^{i-1} j^{-1} \mathbf{R}^{i-1} \mathbf{p}_i, \quad (11)$$

$${}^i \boldsymbol{\omega}_i = {}^{i-1}_i \mathbf{R}^T [{}^{i-1} \boldsymbol{\omega}_{i-1} + \dot{\gamma}_i \hat{\mathbf{k}}], \quad (12)$$

$${}^i \dot{\boldsymbol{\omega}}_i = {}^{i-1}_i \mathbf{R}^T [{}^{i-1} \dot{\boldsymbol{\omega}}_{i-1} + {}^{i-1} \boldsymbol{\omega}_{i-1} \times \dot{\gamma}_i \hat{\mathbf{k}} + \ddot{\gamma}_i \hat{\mathbf{k}}], \quad (13)$$

$${}^i \ddot{\mathbf{p}}_i = {}^{i-1}_i \mathbf{R}^T [{}^{i-1} \dot{\boldsymbol{\omega}}_{i-1} \times {}^{i-1} \mathbf{p}_i + {}^{i-1} \boldsymbol{\omega}_{i-1} \times ({}^{i-1} \boldsymbol{\omega}_{i-1} \times {}^{i-1} \mathbf{p}_i) + {}^{i-1} \ddot{\mathbf{p}}_{i-1}], \quad (14)$$

$${}^i \mathbf{g} = {}^{i-1}_i \mathbf{R}^{i-1} \mathbf{g}. \quad (15)$$

In the equations above, \mathbf{p} is the position of the origin of the reference frame, $\boldsymbol{\omega}$ is the angular velocity of the reference frame, and \mathbf{g} is the gravity. $\hat{\mathbf{k}}$ is the unit vector of the z -axis and \times is the cross product. Equation (14) is the description of the body acceleration. As shown, the second derivative of the joint angle ($\ddot{\gamma}$) appears in this equation. Since, body acceleration is measured by the accelerometer, this formulation not only improves the measurement model, but it provides observability for the second derivative of the joint vector. Consequently, the linearization order of the process model can be increased by one. Based on this formulation, the measurement vector is defined as:

$$\mathbf{z} = [{}^u \boldsymbol{\omega}_{u6} \quad {}^f \boldsymbol{\omega}_{f9} \quad {}^u \mathbf{a}_{u6} \quad {}^f \mathbf{a}_{f9} \quad {}^0 \mathbf{p}_5 \quad {}^0 \mathbf{p}_7]^T. \quad (16)$$

In the equation above, ${}^6 \boldsymbol{\omega}_{u6}$ and ${}^9 \boldsymbol{\omega}_{f9}$ are, respectively, upper arm and forearm gyroscope measurements. Similarly, ${}^6 \mathbf{a}_{u6}$ and ${}^9 \mathbf{a}_{f9}$ are total acceleration measurements of the upper arm and forearm accelerometer. Total accelerations are sum of the gravity acceleration and body acceleration as:

$${}^u \mathbf{a}_{u6} = {}^u \mathbf{g} + {}^u \ddot{\mathbf{p}}_{u6}, \quad (17)$$

$${}^f \mathbf{a}_{f9} = {}^f \mathbf{g} + {}^f \ddot{\mathbf{p}}_{f9}. \quad (18)$$

${}^0 \mathbf{p}_5$ and ${}^0 \mathbf{p}_7$ are, respectively, the position of the elbow and wrist measured by the position sensor.

The measurement noise covariance matrix is defined as:

$$\mathbf{R} = \begin{bmatrix} \sigma_\omega^2 \mathbf{I}_6 & \mathbf{0}_6 & \mathbf{0}_6 \\ \mathbf{0}_6 & \sigma_a^2 \mathbf{I}_6 & \mathbf{0}_6 \\ \mathbf{0}_6 & \mathbf{0}_6 & \sigma_p^2 \mathbf{I}_6 \end{bmatrix}. \quad (19)$$

In this equation, the measurement noise variances for angular velocity, acceleration, and position are respectively designated by σ_ω^2 , σ_a^2 , and σ_p^2 .

3. Simulations

The simulation studies are performed to quantitatively analyze contribution of each error source to joint angle error in a legitimate setting. Then the proposed methods are applied to quantify their effectiveness in mitigating the error.

Table 5 shows the filter design parameters.

Sensor noise variances are determined based on the on-bench samples for Shimmer2RTM Kinematics module (<http://www.shimmer-research.com/>) and KinectTM (<http://www.xbox.com/en-US/kinect>). Shimmer2RTM is the IMU, and KinectTM is the position measurement sensor used in this work. Figure 3 shows the sensor's on-bench data samples compared to the synthetic data samples generated for the purpose of simulation. As shown in Fig. 3(a) due to the lack of a reference vector for angular velocity, the manufacturer's procedure for gyroscope calibration is prone to bias.

The process noise variance is chosen by trial and error. Increase in the variance, leads to a faster filter response and accounts for the mismodeling problems.²⁰ On the other hand, large variance brings about filter instability and high error variance in benign tracking conditions. Since higher accelerations are expected in rehabilitation, $\sigma_{\ddot{\theta}}^2$ should be chosen relatively higher than other applications. The sampling time-step is chosen to be 1 ms which is compatible with common choices in

Table 5. Filter design parameters.

Parameter	Entry	Parameter	Entry
$\sigma_{\ddot{\theta}}^2$	1 ($^{\circ}/s^2$) ²	σ_p^2	10 ⁻⁴ (m) ²
σ_{ω}^2	10 ⁻¹ ($^{\circ}/s$) ²	σ_a^2	10 ⁻² (m/s) ²

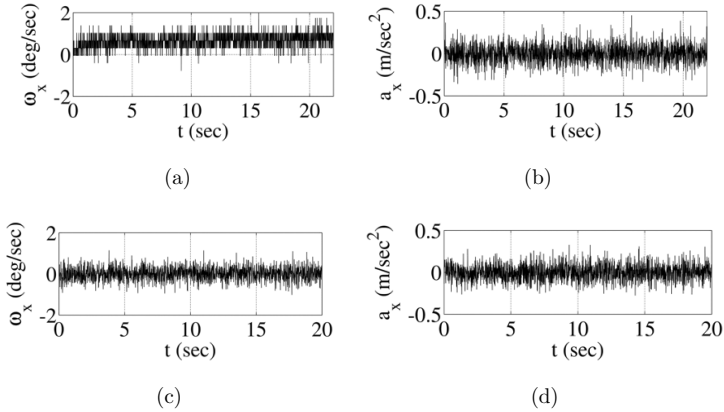


Fig. 3. Stationary sensor data sample. (a) Gyroscope experimental data, (b) accelerometer experimental data, (c) gyroscope simulation data and (d) accelerometer simulation data.

the literature.²¹ The filters are implemented on a 3.20 GHz CPU computer with 32.0 GB RAM.

Simulations are performed by considering one segment (shoulder and upper arm). A sinusoidal trajectory is applied to shoulder flexion/extension angle (θ_0 in Fig. 2) with 90° amplitude and different frequencies representing the speed of motion. The simulation studies are presented in three parts, studying linearization error, sensor-to-segment misalignment error, and body acceleration perturbations, respectively. Simulation protocols specific to each subsection are presented in the corresponding subsection.

3.1. Linearization errors

This simulation quantifies the linearization error considering three measurement models: Inclinometer Model, Inclinometer/Gyroscope Model, and Accelerometer/Gyroscope Model. Moreover, performance of EKF and UKF are compared for each measurement model. To exclude the effect of the body acceleration perturbations on the joint angle error sensor is located on the shoulder center of rotation, so body acceleration is zero. The synthetic measurements are then filtered based on three measurement models: Inclinometer Model, Inclinometer/Gyroscope Model, and Accelerometer/Gyroscope Model. Figure 4 shows the simulation results for a sinusoidal motion with 1 Hz frequency. The inclinometer model has zero-order observability of the inclination angle. In other words, it has information about the inclination angle, but not about its higher order derivatives. As shown, estimation of the inclination angle based merely on the inclinometer information has a considerable error when used for a dynamic application where higher order derivatives are significant. By measuring the angular velocity, the gyroscope provides first-order observability and improves the linearization error. As a result gyroscopes is, today, an integral part of all orientation tracking systems. Similarly, body acceleration measurements of the accelerometer is used in this work to provide second-order observability. As shown, the second-order observability is sufficient to eliminate the linearization error for a movement which is typical of the rehabilitation applications.

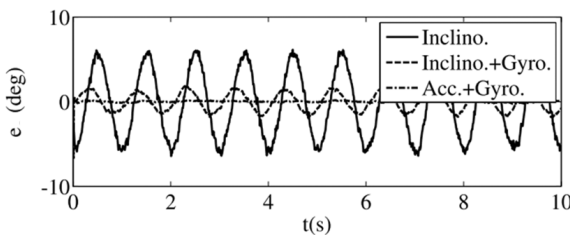


Fig. 4. Comparison of the inclination angle error for a sinusoidal motion with 1 Hz frequency. Solid: Zero-order linearization (Inclinometer Model), Dashed: first-order linearization (Inclinometer/Gyroscope Model), Dash-dot: second-order linearization (Accelerometer/Gyroscope Model).

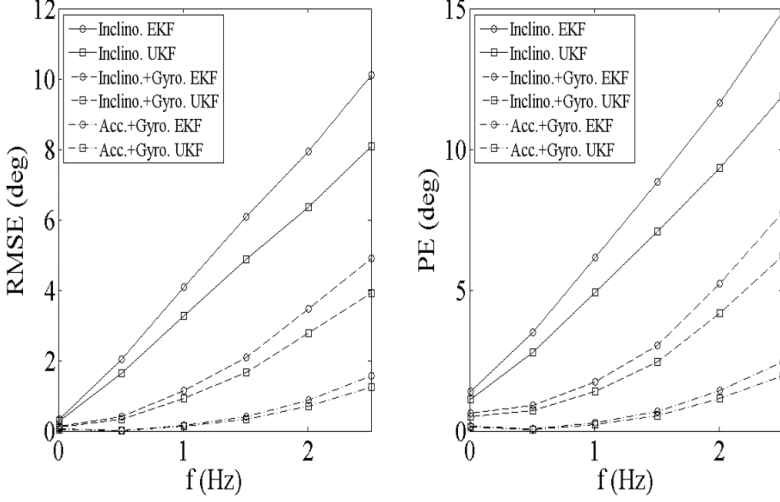


Fig. 5. Influence of process model linearization order on the joint variable error and its sensitivity to frequency.

To investigate the sensitivity of each measurement model to the dynamics of the reference motion, the previous simulation is repeated with frequency ranging from 0 to 2.5 Hz. As shown in Fig. 5, both linearization error and its sensitivity to the motion dynamics are significantly lower in the proposed method. EKF is the most common non-linear filter because of its simplicity which translate to higher speed using a certain computing resource and less memory. Its application is merely limited by linearization in this algorithm, especially for highly dynamic movements and large sampling intervals.²² Otherwise, it is preferred to more complex filters such as Unscented Kalman Filter (UKF) because it is simpler, can provide higher speed and requires less memory, especially for real-time applications. As such, the proposed approach can expands EKF's scope of work in real-time rehabilitation applications by removing this limitation.

3.2. Sensor-to-segment misalignment errors

In this section, we characterize the sensitivity of the joint angle error to sensor-to-segment misalignment. To account for the non-linearity of the model, simulations are performed both in static and dynamic conditions with different speed of the reference motion. The speed is characterized by the frequency of the reference sine wave. The usefulness of using position measurements to correct for such this error is quantified and discussed.

In Fig. 6, the solid line and the dash-dot line shows the steady state error with $+10^\circ$ initialization error for a static test in which unit perturbations are imposed on the accelerometer and gyroscope, respectively. As shown, fusion of the information from the accelerometer with gyroscope prevents drifting error in the presence of

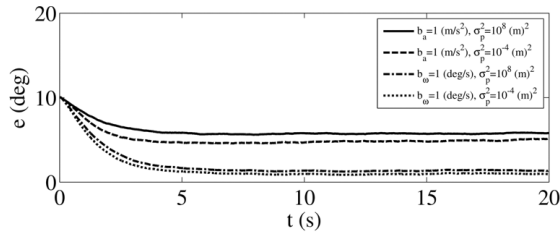


Fig. 6. Static simulation; inclination angle error per unit perturbations in IMU with and without correcting effect of the position measurement.

gyroscope bias. As shown, the correcting effect of the position measurements is deactivated by setting the estimate of the position measurement noise variance to infinity (10^8). A unit perturbation in the accelerometer and gyroscope, respectively, leads to 5.7° and 1.3° steady-state inclination angle error in a static simulation. The dashed line and the dotted line show the errors when position measurement is activated. By engaging the position measurement, the steady-state error is mitigated by 15% (5.7° to 4.8°) for accelerometer perturbations and by 30% (1.3° to 0.9°) for gyroscope perturbations.

To explore the impact of position measurement accuracy on mitigating the sensor-to-segment misalignment error of the IMU, the simulation has been repeated using synthetic position measurements with 1 mm ($\sigma_p^2 = 10^{-6} \text{ m}^2$) to 1 m ($\sigma_p^2 = 1 \text{ m}^2$) accuracy. As shown in Fig. 7, the accuracy of Kinect ($\sigma_p^2 = 10^{-4} \text{ m}^2$) is weakly sufficient to make any improvements; however, future accomplishments in

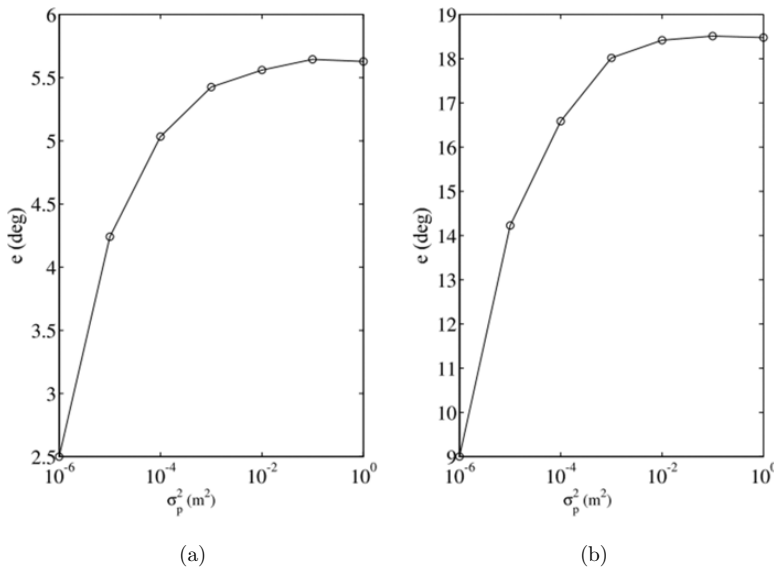


Fig. 7. The influence of position measurement accuracy on the correction of inertial measurement perturbations.

the low-cost markerless position measurement technology, beyond Kinect's accuracy, can have an important impact on the effectiveness of this approaches.

The dynamic simulations in this part are performed to characterize behavior of the sensor-to-segment misalignment errors with motion dynamics. This behavior stems from the non-linearity of the measurement model. In this simulation, unit perturbations are imposed on the accelerometer and gyroscope in a shoulder flexion/extension motion. The motion is a sinusoidal trajectory with 90° amplitude and frequency ranging from 0 Hz to 3 Hz.

In the first simulation, the correcting effect of the position measurements is deactivated by setting the estimate of the position measurement noise variance to infinity (10^8). The results of this simulation are shown by solid lines in Fig. 8. As shown, the dynamic error is lower than static error, and it decreases until 1 Hz. Beyond this frequency, the error increases again. Comparison of the curves with the "No Perturbation" curve suggests that at high frequency, the error is mainly due to the process model linearization. The "No Perturbation" curve is the same as Accelerometer/Gyroscope Model case in Fig. 5. At low frequencies, the process model linearization error is negligible, and the effect of unit measurement perturbations is high. As frequency increases, the inclination angle error due to unit measurement perturbations decreases; however, the process model linearization error dominates and increases the total error. The reduction of the inclination angle error due to unit measurement perturbations with frequency is due to the proportionality of the Kalman gain to the inverse of the local measurement matrix. Instead, the linearization effects become significant. Based on this simulation, the optimum operating point of this algorithm is the 1 Hz frequency.

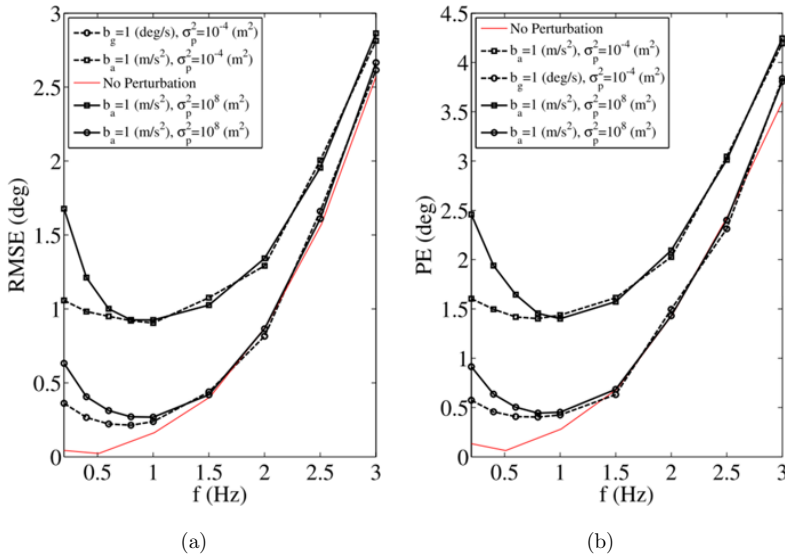


Fig. 8. Dynamic simulation; inclination angle error behavior with frequency.

The Dashed lines in Fig. 8 represent the results of the correcting effect of the position measurements activated ($\sigma_p^2 = 10^{-4} \text{ m}^2$). Simulation results indicate when frequency of the motion increases, the position measurement lose its effectiveness in correcting for the sensor-to-segment misalignment error of the IMU; however, typical upper limb rehabilitation tasks are within scope of its effectiveness. This simulation demonstrates that the low-cost markerless optical position sensing technology has the potential to mitigate the only prominent practical limitation of the inertial approach that is sensor-to-segment misalignment.

3.3. Body acceleration error

This section is dedicated to quantification of the body acceleration error and comparison between the proposed compensation method and common competing compensation techniques. To consider body acceleration, the sensor is located far from the shoulder center of rotation near elbow. A typical shoulder flexion/extension rehabilitation task has been represented with a sinusoidal trajectory with 90° amplitude and 1 Hz frequency.

The proposed approach (Method A) is compared, in terms the body acceleration compensation, with a common competing technique (Method B) and a case in which the body acceleration is not compensated (Method C). Methods B and C are both based on the Inclinometer/Gyroscope Model where the position of the sensor relative to the joint center of rotation is not considered. Method B performs body acceleration compensation using state augmentation technique. In this method, body acceleration is added to the state vector as a state variable with its dynamics modeled as a GM-1 process.¹⁷

Figure 9 shows the inclination angle error from the three methods. Mean and peak error in each approach are tabulated in Table 6.

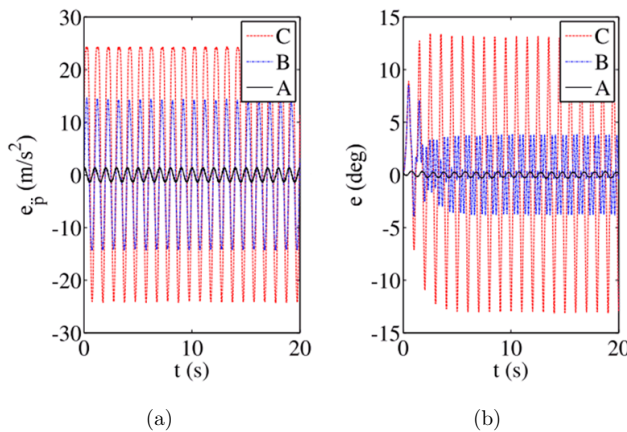


Fig. 9. (a) Body acceleration compensation error. (b) Inclination angle error.

Table 6. Body acceleration compensation performance in simulation.

Method	RMSE		PE	
	Mean	Std	Mean	Std
A	0.20°	0.02°	0.35°	0.02°
B	2.51°	0.51°	8.48°	0.74°
C	7.39°	0.23°	13.43°	0.62°

As shown in Method C, if not compensated, the body acceleration perturbations bring about significant error in typical task. This error is one order of magnitude more significant than the linearization error. More quantitatively, Table 6 shows that for a typical task the body acceleration perturbation can contribute about 7° and 13° to Root Mean Square Error (RMSE) and Peak Error (PE), respectively. Comparing the results of proposed method (Method A) with Method B, simulations demonstrate improvements in body acceleration compensation. As shown in Table 6, for a typical task this improvement is about 2° RMSE and 8° PE. This improvement stems from the fact that the proposed method models body acceleration considering its relationship the joint angle variables, while on the other hand, Method B models the body acceleration as an independent state variable. Even though there is this fundamental advantage in the proposed method over Method B, it should be pointed out that the proposed method is merely applicable to tasks where trunk is stationary. This happens quite often in upper limb rehabilitation tasks, however in a general ambulatory task this method is not directly applicable. On the other hand, Method B does not have such a requirement and can be applied to a more general movements. This means that prior information about the type of movement can be exploited to improve the accuracy and performance of the trackers.

4. Experiments

The experiments section validates the quantitative results obtained in simulations in the real setting. The experiment is performed on a mechanical upper limb stroke rehabilitation device also known as shoulder wheel. The equipment consists of a wooden rotary wheel with a handle whose radial distance from the wheel center can be adjusted. The shaft’s rotation angle is encoded. Figure 10(a) shows the rotary wheel as well as the test subject’s configuration during the test. The idea of the experiment is to derive the inverse kinematics for this specific configuration and use it as the reference to quantify the accuracy. This section encompasses two subsections. The first subsection presents the derivation of the inverse kinematics and the second subsection presents results and discussion.

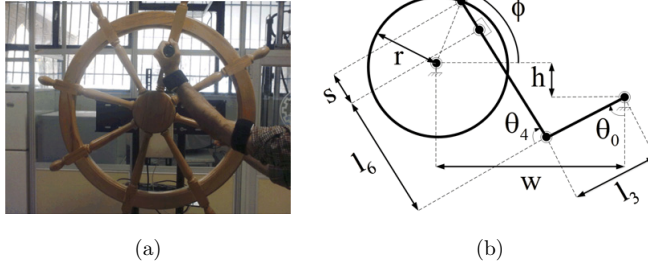


Fig. 10. (a) Shoulder Wheel test setup. (b) The kinematic model of the Shoulder Wheel test setup.

4.1. Inverse kinematics

Figure 10(b) shows the kinematic model for the test setup. This model is used to perform an inverse kinematic analysis. More specifically, the inverse kinematics analysis involves deriving analytical relationship for the flexion/extension joint angles of the shoulder and elbow as functions of the shaft rotation angle. Equations (20) and (21) shows these equations:

$$\theta_0^* = 2\pi - [a \tan 2(r \sin \phi + h, r \cos \phi - w) - a \tan 2((s + l_6) \sin \theta_4^*, l_3 + (s + l_6) \cos \theta_4^*)], \quad (20)$$

$$\theta_4^* = \frac{3\pi}{2} - a \cos \left[\frac{(r \cos \phi - w)^2 + (r \sin \phi + h)^2 - l_3^2 - (s + l_6)^2}{2l_3(s + l_6)} \right]. \quad (21)$$

Requirements for the validity of (20) and (21) in the experimental setup is that the subject's wrist joint is fixed and shoulder has no abduction/adduction movements. This constraint was satisfied by resting the elbow on the wheel.

Comparing the upper limb kinematic model (Fig. 2) with the test setup kinematic model (Fig. 10), the reference joint vector is:

$$\theta^* = [\theta_0^* \ 0 \ 0 \ \theta_4^* \ \pi/2]^T. \quad (22)$$

The geometrical parameters of the subject and sensor installation are listed in Table 7. The entries for w and h are obtained by averaging the position data for the shoulder and the center of the wheel. Other geometrical parameters are measured by a Vernier caliper. The z -axis of the upper arm IMU is aligned with the elbow

Table 7. Geometrical parameters.

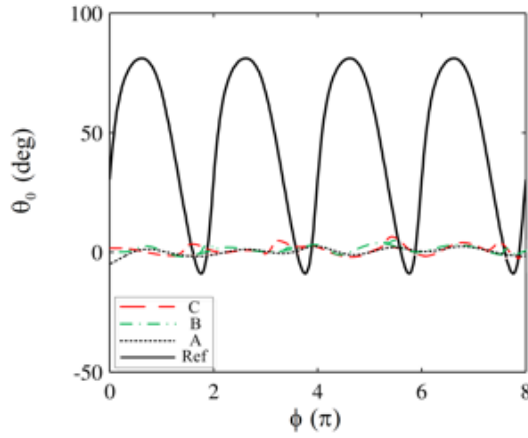
Parameter	Entry	Parameter	Entry
l_{u3}	11 cm	l_{f6}	20 cm
θ_{u4}	$\pi/2$	θ_{f7}	$\pi/2$
l_{u5}	2 cm	l_{f8}	1 cm
l_3	22 cm	l_6	20 cm
w	25 cm	h	5 cm
r	15 cm	s	4 cm

flexion/extension axis $\theta_{u4} = \pi/2$. The x -axis of the forearm IMU is aligned with the wrist flexion/extension axis $\theta_{f7} = \pi/2$.

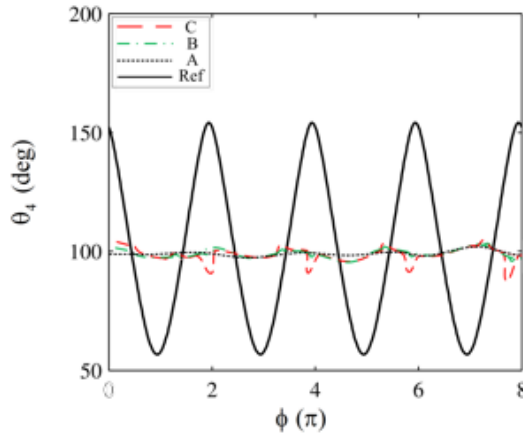
4.2. Results and discussion

In this subsection, first the improvements of body acceleration compensation is validated. Then, the effectiveness of the Kinect sensor is tested experimentally. Finally, a performance of EKF and UKF are compared and discussed.

In Fig. 11, the solid line shows the inverse kinematic solutions as the reference. Joint angle errors based on Methods A, B, and C are computed based on this reference and compared with each other.



(a)



(b)

Fig. 11. Shoulder and elbow flexion/extension angle error. Solid: reference value. Dotted: error with Method A. Dash-dot: error with Method B. Dashed: error with Method C.

Table 8. Shoulder flexion/extension angle error.

Method	RMSE		PE	
	Mean	Std	Mean	Std
A ($\sigma_p^2 = \infty$)	4.9°	1.0°	6.0°	1.1°
A ($\sigma_p^2 = 10^{-4}$)	4.8°	1.3°	6.1°	0.9°
B	5.5°	1.3°	6.8°	1.5°
C	7.1°	2.3°	13.8°	1.0°

Table 8 shows the mean and peak error of the competing methods, statistically, based on three trials. The experimental results confirms the improvements in the body acceleration compensation compared to Method B. The improvements in experiments are less compared to simulations. This can be partly attributed to the fact that the reference motion is not an ideal sine wave. As shown, elbow flexion/extension error is significantly greater than shoulder flexion/extension error. The estimates of the elbow joint angles are based on the measurements of the forearm IMU. Since the forearm IMU is located in a father distance from the global reference frame than the upper arm IMU, modeling error is propagated in its measurement model. Moreover, magnitudes of the main signals measured by the forearm IMU are greater than the upper arm IMU; so, sensor-to-segment misalignment error is greater for elbow joint angles.

To evaluate the effect of using Kinect in real conditions, Method A is applied once by ignoring Kinect measurements ($\sigma_p^2 = \infty$) and once by considering it ($\sigma_p^2 = 10^{-4}$). Results of this experiment are shown in the second row of Table 8. Unlike simulations, experiment results does not show significant improvement in RMSE; however, confidence of the estimates are increased as suggested by consistently lower standard deviations. The fact that under real conditions Kinect did not performed as effective as simulations can be attributed to the fact that its accuracy is probably lower under dynamic conditions compared to static conditions. That being said, future improvements in the technology of low-cost markerless sensing will increase effectiveness of this method in improving the accuracy.

The results in the first and second row are corresponding to Method A ($\sigma_p^2 = \infty$) in Tables 8 and 9, respectively. To compare the performance of EKF with UKF, the experimental measurements are filtered with UKF using the same filter parameters.

Table 9. Elbow flexion/extension angle error.

Method	RMSE		PE	
	Mean	Std	Mean	Std
A ($\sigma_p^2 = \infty$)	5.9°	1.1°	7.2°	1.7°
A ($\sigma_p^2 = 10^{-4}$)	6.1°	0.9°	7.1°	1.3°
B	7.4°	2.8°	10.3°	2.5°
C	10.2°	2.3°	19.1°	3.1°

Table 10. Angle errors of Method A using UKF.

Joint	RMSE		PE	
	Mean	Std	Mean	Std
Shoulder	4.7°	0.9°	5.9°	0.8°
Elbow	5.9°	1.0°	6.9°	1.4°

Table 10 shows the mean and peak error obtained by UKF based on three trials. As shown, the performance is slightly better; however, this slight improvement is at cost of a more complex filter with slower speed and higher memory necessary which might not be favorable in real-time applications.

5. Conclusions

This work attempts to improve the upper limb joint angle estimation in dynamic tasks such as in stroke patient rehabilitation by focusing on linearization errors, body acceleration perturbation errors, and sensor-to-segment misalignment errors. Linearization errors, body acceleration perturbation errors are dealt with modeling body acceleration. Low-cost markerless optical position measurements are applied as an attempt to correcting for sensor-to-segment misalignment.

The body acceleration is modeled based on a combination of the DH convention and 3D rigid body kinematics equations. According to the results, proposed modeling improves accuracy significantly by compensating for the body acceleration. According to the simulation results, improvements achieved by compensating body acceleration can be more than 2° RMSE and 8° PE compared common competitive methods. In experiment, the improvement is 0.6° RMSE and 0.8° PE for shoulder and 1.5° RMSE and 3.1° PE for elbow. Moreover, body acceleration model exploits the body acceleration measurements of the accelerometer increasing linearization order. Improved linearization provides a better opportunity for employing common non-linear filters such as EKF that are much simpler and faster which in turn improves the real-time performance the algorithm. While significant in simulations, empirical evidence suggests that the use of Kinect only improves the certainty of the results that is statistically more confident estimates but the accuracy is not affected significantly.

References

1. Zhou H, Hu H, Human motion tracking for rehabilitation — A survey, *Biomed Signal Process Control* **3**(1):1–18, 2008.
2. Roux E *et al.*, Evaluation of the global optimisation method within the upper limb kinematics analysis, *J Biomech* **35**(9):1279–1283, 2002.
3. Welch G, Foxlin E, Motion tracking: No silver bullet, but a respectable arsenal, *IEEE Comput Graphics Appl* **22**(6):24–38, 2002.

4. Fang L *et al.*, Design of a wireless assisted pedestrian dead reckoning system-the Nav-Mote experience, *IEEE Trans Instrum Meas* **54**(6):2342–2358, 2005.
5. Bouten CVC *et al.*, A triaxial accelerometer and portable data processing unit for the assessment of daily physical activity, *IEEE Trans Biomed Eng* **44**(3):136–147, 1997.
6. Liu K *et al.*, Novel approach to ambulatory assessment of human segmental orientation on a wearable sensor system, *J Biomech* **42**(16):2747–2752, 2009.
7. Bagala F *et al.*, Calibrated 2D angular kinematics by single-axis accelerometers: From Inverted pendulum to-link chain, *IEEE Sens J* **12**(3):479–486, 2012.
8. Veltink PH *et al.*, Detection of static and dynamic activities using uniaxial accelerometers, *IEEE Trans Rehabil Eng* **4**(4):375–385, 1996.
9. Roetenberg D, Inertial and magnetic sensing of human motion, University of Twente, 2006.
10. Peng C, Oelmann B, Joint-angle measurement using accelerometers and gyroscopes — A survey, *IEEE Trans Instrum Meas* **59**(2):404–414, 2010.
11. Dejnabadi H, Jolles BM, Aminian K, A new approach to accurate measurement of uniaxial joint angles based on a combination of accelerometers and gyroscopes, *IEEE Trans Biomed Eng* **52**(8):1478–1484, 2005.
12. Bergmann JH, Mayagoitia RE, Smith IC, A portable system for collecting anatomical joint angles during stair ascent: A comparison with an optical tracking device, *Dyn Med* **8**(1):3, 2009.
13. Usta UY, Comparison of quaternion and euler angle methods for joint angle animation of human figure models, DTIC Document, 1999.
14. Frey W, Application of inertial sensors and flux-gate magnetometer to real-time human body motion capture, Thesis, Naval Postgraduate School, Monterey, California. 1996.
15. Rehbindler H, Hu X, Drift-free attitude estimation for accelerated rigid bodies, *Automatica* **40**(4):653–659, 2004.
16. Ladetto Q, Merminod B, In step with INS: Navigation for the blind, tracking emergency crews, *GPS World* **13**(10):30–38, 2002.
17. Sabatini AM, Quaternion-based extended Kalman filter for determining orientation by inertial and magnetic sensing, *IEEE Trans Biomed Eng* **53**(7):1346–1356, 2006.
18. Zhang Z, Wong WC, Wu J, Wearable sensors for 3D upper limb motion modeling and ubiquitous estimation, *J Control Theo Appl* **9**(1):10–17, 2011.
19. Craig JJ, Manipulator Kinematics, in *Introduction to Robotics: Mechanics and Control*, Addison-Wesley, 2004, pp. 75–83.
20. Maybeck PS, *Stochastic Models, Estimation, and Control*, Academic Press, 1982.
21. Sabatini AM, Kalman-filter-based orientation determination using inertial/magnetic sensors: Observability analysis and performance evaluation, *Sensors* **11**(10):9182–9206, 2011.
22. Crassidis JL, Markley FL, Unscented filtering for spacecraft attitude estimation, *J Guid Control Dyn* **26**(4):536–542, 2003.